



# Effect of micro- $\text{Al}_2\text{O}_3$ powders on oxidation and corrosion behaviors of low-carbon MgO–C refractories

Yang Chen<sup>1,2</sup> · Zeng-yi Li<sup>1</sup> · Hao-bo Tan<sup>1</sup> · Yu-ran Fu<sup>1</sup> · Jun Ding<sup>2</sup> · Cheng-ji Deng<sup>2</sup> · Chao Yu<sup>2</sup>

Received: 24 November 2023 / Revised: 28 November 2023 / Accepted: 31 December 2023 / Published online: 2 April 2024  
© China Iron and Steel Research Institute Group Co., Ltd. 2024

## Abstract

To solve the problem of poor high-temperature service performance caused by low carbonization of MgO–C refractories, low-carbon MgO–C refractories with excellent thermal shock, oxidation and corrosion resistances were successfully designed by using SiC whiskers as reinforcing phases and introducing micro- $\text{Al}_2\text{O}_3$  powders as additives. The results indicated that the addition of micro- $\text{Al}_2\text{O}_3$  powders optimized the internal structure of the material, like the columnar  $\beta$ - $\text{Si}_3\text{N}_4$  with a stepped distribution and the mosaic structure formed between granular and flaky  $\text{Mg}_2\text{SiO}_4$ , which synergistically strengthened and toughened the material and gave the material excellent mechanical properties and thermal shock resistance. Specifically, the cold modulus of rupture and cold crushing strength after thermal shock were increased by 4.1 and 20.3 MPa, respectively. Moreover, the addition of micro- $\text{Al}_2\text{O}_3$  powders promoted the formation of fine particles of  $\text{Mg}_2\text{SiO}_4$ ,  $\text{MgAl}_2\text{O}_4$  and MgO, as well as a dense protective layer of  $\text{Mg}_2\text{SiO}_4$  in the material under high-temperature environment. Furthermore, spinel and high-temperature solid solution were formed in the corrosion environment. The oxidation and corrosion resistances were greatly improved by 41% and 15%, respectively.

**Keywords** Low-carbon MgO–C refractory · Oxidation resistance · Corrosion resistance · Thermal shock resistance · Micro- $\text{Al}_2\text{O}_3$  powder

## 1 Introduction

The consumption and production of iron and steel are closely related to the development of national economy and the process of industrialization, and the refractory is an important support for high-temperature industry [1–4]. At present, the theme of economic and social development is to promote high-quality development. The iron and steel industry pays more attention to variety and quality, green,

low-carbon, and innovative development [5–7]. This also puts forward higher requirements for carbon-containing refractories closely related to the iron and steel industry.

MgO–C refractory, as an indispensable basic material in the process of smelting including refining process, has an irreplaceable position [8–10]. With the increasing demand for clean steel in recent years, the development of low-carbon MgO–C refractories has become a research hotspot in this field, but the outstanding problems of poor thermal shock stability and slag corrosion resistance caused by low carbonization have emerged [11–14]. In addition, like all carbon-containing refractories, low-carbon MgO–C refractories still face the problem of poor oxidation resistance [15–18]. Recently, in the work of reducing graphite content, starting from the synergistic improvement in the comprehensive performance of low-carbon MgO–C refractories, the in-situ formation of ceramic phases has shown good potential and advantages. The introduced additives generate ceramic phase in situ in the process of heat treatment or use of refractories, and their volume expansion effect reduces the pore volume, which prevents

✉ Yang Chen  
chenyang\_9210@163.com

✉ Jun Ding  
dingjun@wust.edu.cn

✉ Cheng-ji Deng  
cjdeng@wust.edu.cn

<sup>1</sup> School of Materials Science and Engineering, Hunan Institute of Technology, Hengyang 421002, Hunan, China

<sup>2</sup> The State Key Laboratory of Refractories and Metallurgy, Wuhan University of Science and Technology, Wuhan 430081, Hubei, China

the penetration of slag and molten steel into the material and improves the thermomechanical properties of the refractories while enhancing oxidation and corrosion resistances [19–21]. For example, Ren et al. [22] used Al<sub>2</sub>O<sub>3</sub> as a reinforcer and La<sub>2</sub>O<sub>3</sub> as a modifier to generate MgAl<sub>2</sub>O<sub>4</sub> (whisker-like and granular morphologies), Mg<sub>2</sub>SiO<sub>4</sub> (whisker-like and granular morphologies) and 2CaO·4La<sub>2</sub>O<sub>3</sub>·6SiO<sub>2</sub> (rod-like morphology) ceramic phases in MgO–C refractories. The volume expansion and intergranular phase enhancement effects produced by these ceramic phases increased the oxidation, thermal shock and corrosion resistances of the refractories by 14%, 18% and 43%, respectively. In our early work [23, 24], we used Si powder/resin as catalyst supports via impregnation method, and MgO–C refractories were prepared by high-temperature catalytic nitridation. The morphological evolution, generation and distribution of MgSiN<sub>2</sub> and Si<sub>3</sub>N<sub>4</sub> were controlled by regulating the nitriding temperature and catalyst content, so that the long conical MgSiN<sub>2</sub> and columnar Si<sub>3</sub>N<sub>4</sub> were pinned in the aggregate and matrix to form an interlocking ceramic network structure, which improved the mechanical properties, thermal shock and corrosion resistances of refractories. It can be found that the controllable formation of ceramic phases is an effective method to improve the properties of materials, and it is expected to achieve the synergistic improvement in thermomechanical properties, corrosion and oxidation resistances of low-carbon MgO–C refractories.

Recently, we [25] introduced SiC whiskers loaded with catalyst into low-carbon MgO–C refractories, which improved the effect of prepared SiC whiskers containing crystal defects on the properties of materials to a certain extent and promoted the formation of columnar β-Si<sub>3</sub>N<sub>4</sub> and flaky Mg<sub>2</sub>SiO<sub>4</sub>, thereby improving the thermomechanical strength of the materials. Unfortunately, the introduction of more SiC whiskers brought problems such as low strength, high apparent porosity, poor oxidation and corrosion resistances, especially high-temperature service performance, which limited its industrial application. Relevant studies [26–29] have confirmed that the introduction of micron-sized Al<sub>2</sub>O<sub>3</sub> powders into MgO–C refractories can improve the porosity of the material by its size effect. Furthermore, micron-sized Al<sub>2</sub>O<sub>3</sub> powders can form MgAl<sub>2</sub>O<sub>4</sub> phase with high melting point, high strength and alkaline slag corrosion resistance during high-temperature service, which can improve the thermomechanical properties, oxidation and corrosion resistances of the material.

Based on the above ideas, aiming at the problem that the low carbonization of MgO–C refractories leads to poor high-temperature service performance, we used SiC whiskers loaded with catalysts as the reinforcing phase and expected to design low-carbon MgO–C refractories with excellent high-temperature service performance (thermal

shock, oxidation and corrosion resistances) by introducing micro-Al<sub>2</sub>O<sub>3</sub> powders. The positive effects of micro-Al<sub>2</sub>O<sub>3</sub> powders on the microstructure and high-temperature properties of MgO–C refractories were studied. In particular, the effects of the addition of micro-Al<sub>2</sub>O<sub>3</sub> powders on the high-temperature oxidation and corrosion behaviors of MgO–C refractories were systematically investigated.

## 2 Experimental

### 2.1 Raw materials

The raw materials of the refractories included fused magnesia aggregate (MgO ≥ 97.0 wt.%, 1–3 mm and ≤ 1 mm, Gongyi Jinfeng Water Purification Material Co., Ltd., China), fused magnesia powder (MgO ≥ 97.0 wt.%, ≤ 0.074 mm, Gongyi Jinfeng Water Purification Material Co., Ltd., China), flake graphite (C ≥ 97.0 wt.%, ≤ 0.15 mm, Gongyi Jinfeng Water Purification Material Co., Ltd., China), Si powder (Si ≥ 99.9 wt.%, ≤ 0.074 mm, Qinghe County Xintie Metal Co., Ltd., China), micro-Al<sub>2</sub>O<sub>3</sub> powders (Al<sub>2</sub>O<sub>3</sub> ≥ 99.99 wt.%, 5–6 μm, Shanghai Aladdin Biochemical Technology Co., Ltd., China), liquid phenolic resin (45.0–48.0 wt.% carbon yield, Jining Huakai Resin Co., Ltd., China), and SiC whiskers loaded with catalyst (Ni(NO<sub>3</sub>)<sub>3</sub>·6H<sub>2</sub>O ≥ 98.0 wt.%, Sinopharm Chemical Reagent Co., Ltd., China). The SiC whiskers were used as additives, and the detailed preparation process can be referred to our previous work [25].

### 2.2 Preparation

According to the formulations in Table 1, the raw materials were mixed evenly and pressed under 200 MPa to make 25 mm × 25 mm × 140 mm strip green bodies, φ50 mm × 50 mm cylindrical green bodies, and φ50 mm × 50 mm crucible green bodies with a hole size

**Table 1** Compositions of MgO–C refractory samples (wt.%)

Raw material	Particle size	Sample S	Sample SL
Fused magnesia	1–3 mm	30	30
	≤ 1 mm	40	40
	≤ 0.074 mm	13	11
Flake graphite	≤ 0.15 mm	4	4
Si powder	≤ 0.074 mm	10	10
SiC whisker	–	3	3
Al <sub>2</sub> O <sub>3</sub> powder	5–6 μm	–	2
Ni(NO <sub>3</sub> ) <sub>3</sub> ·6H <sub>2</sub> O	–	+ 0.1	+ 0.1
Phenolic resin	–	+ 4	+ 4

of  $\phi 20 \text{ mm} \times 18 \text{ mm}$ , and then cured at  $110 \text{ }^\circ\text{C}$  for 24 h. Subsequently, all green bodies were nitrided at high temperatures ( $1350 \text{ }^\circ\text{C}$  for 2 h, and then  $1400 \text{ }^\circ\text{C}$  for 4 h) and under flowing  $\text{N}_2$  ( $\sim 99.999 \text{ vol.}\% \text{ N}_2$ ).

### 2.3 Characterization and testing methods

The phase composition and microstructure of samples were determined by X-ray diffractometry (XRD, Rigaku, SmartLab SE) and field-emission scanning electron microscopy (SEM, ThermoFisher, Apreo S HiVac), respectively.

Referring to the Chinese standards GB/T 2997–2015, GB/T 3001–2017, and GB/T 5072–2008, the apparent porosity (AP), bulk density (BD), cold modulus of rupture (CMOR), and cold crushing strength (CCS) of the refractories were tested, respectively.

For the high-temperature service performance of refractories, the thermal shock resistance test was performed for nitrided strip and cylindrical samples by shocking at  $1100 \text{ }^\circ\text{C}$  for 30 min in air and subsequent twice compressed air quenching with pressure of 0.1 MPa. The refractoriness under load (RUL) test was performed according to the Chinese standard YB/T 370–2016 for nitrided cylindrical samples with compressive load of 0.2 MPa, and the softening temperatures with 0.5% and 0.6% deformation (denoted as  $T_{0.5}$  and  $T_{0.6}$ ) of the maximum expansion value were recorded, respectively. The oxidation resistance test was performed for nitrided cylindrical samples by high-temperature oxidation at  $1400 \text{ }^\circ\text{C}$  for 2 h in air, and the calculation method of oxidation index is given in Eq. (1). The corrosion resistance test was performed for nitrided crucible samples by static crucible method via erosion at  $1400 \text{ }^\circ\text{C}$  for 2 h in air with a slag (36.1 wt.% CaO, 36.0 wt.%  $\text{Al}_2\text{O}_3$ , 10.3 wt.%  $\text{SiO}_2$ , 6.3

wt.% TFe, 5.2 wt.% MgO, and 2.3 wt.% MnO) [25]; and the calculation method of corrosion index is shown in Eq. (2). More details of tests can be found in our earlier work [14, 23, 25].

$$I_{oi} = \frac{A_o}{A_c} \times 100\% \quad (1)$$

where  $I_{oi}$  is the oxidation index, %;  $A_o$  is the oxidation area of the cylindrical sample; and  $A_c$  is the cross-sectional area of the cylindrical sample.

$$I_{ci} = \frac{A_{cc} - A_{ca}}{A_{ca}} \times 100\% \quad (2)$$

where  $I_{ci}$  is the corrosion index, %;  $A_{cc}$  is the corrosion area including the crucible area; and  $A_{ca}$  is the crucible area.

## 3 Results and discussion

### 3.1 Phase composition and microstructural evolution

The XRD patterns of samples S and SL (without micro- $\text{Al}_2\text{O}_3$  and with micro- $\text{Al}_2\text{O}_3$ ) after nitriding were compared. As shown in Fig. 1, MgO, graphite,  $\alpha\text{-Si}_3\text{N}_4$ ,  $\beta\text{-Si}_3\text{N}_4$ , SiC and  $\text{Mg}_2\text{SiO}_4$  phases were detected in sample S. With the addition of micro- $\text{Al}_2\text{O}_3$  powders, a new phase of AlN was detected in sample SL, and the diffraction peak intensity of SiC increased significantly, while the diffraction peak intensities of  $\alpha\text{-Si}_3\text{N}_4$  and  $\text{Mg}_2\text{SiO}_4$  decreased slightly.

The fracture morphologies of samples S and SL nitrided at  $1400 \text{ }^\circ\text{C}$  are shown in Fig. 2. For sample S without micro- $\text{Al}_2\text{O}_3$  powders, many columnar  $\beta\text{-Si}_3\text{N}_4$  grains (average length of  $2.89 \mu\text{m}$ , and average diameter of  $1.41 \mu\text{m}$ ) were formed (Fig. 2a). A large number of chain-

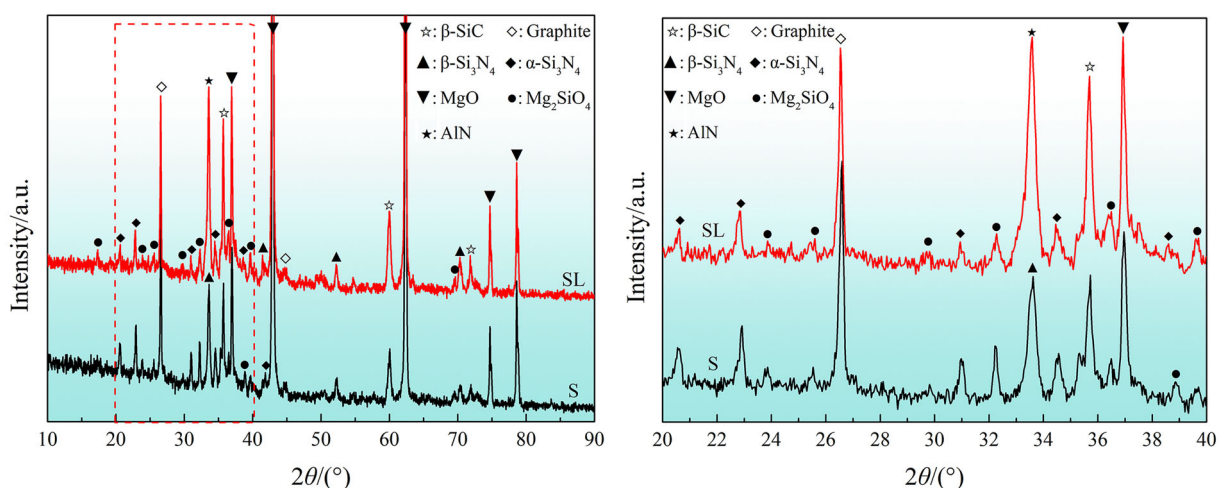
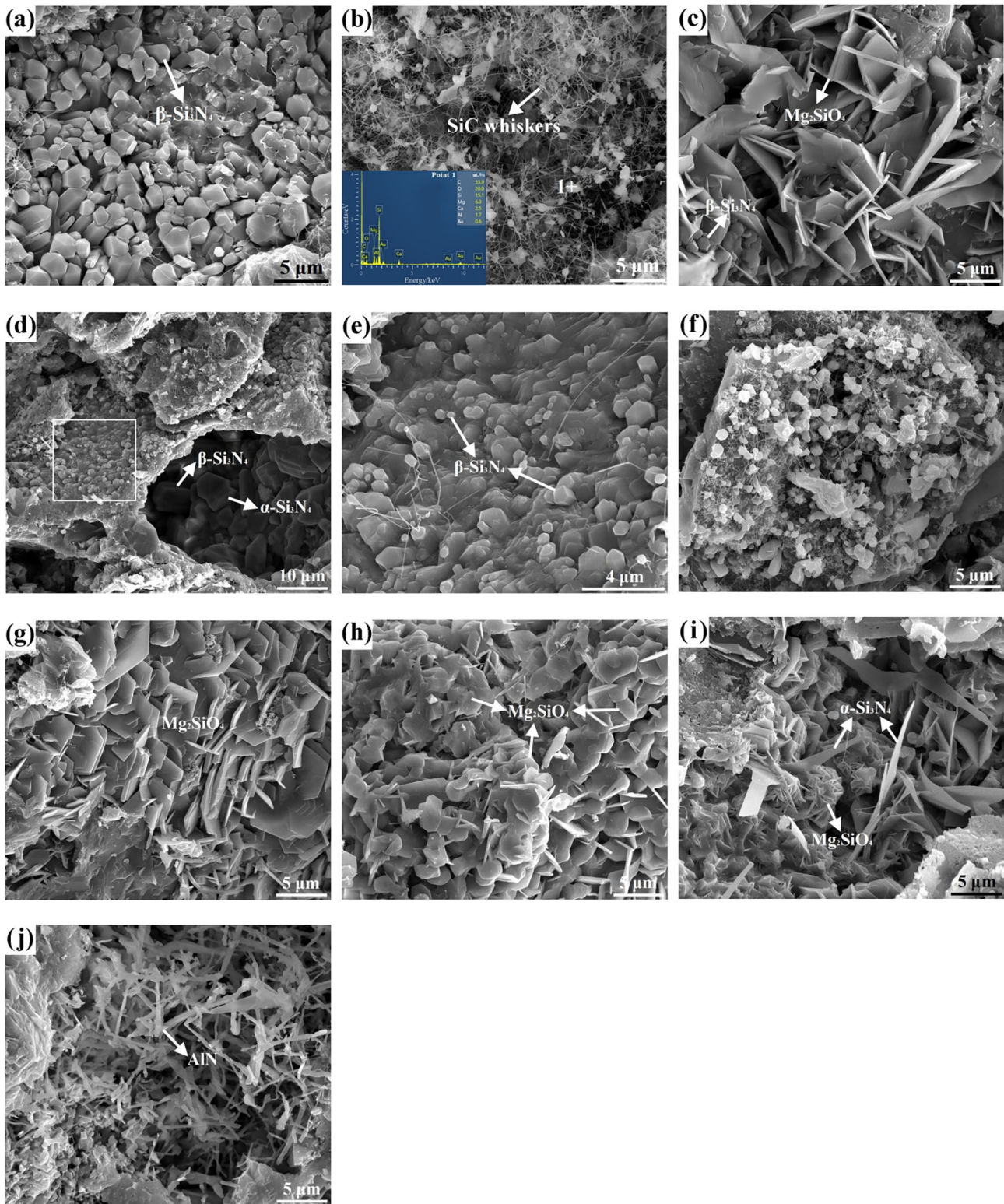


Fig. 1 XRD patterns of samples S and SL nitrided at  $1400 \text{ }^\circ\text{C}$ .  $2\theta$ —Diffraction angle



**Fig. 2** SEM images of samples S (a–c) and SL (d–j) nitrided at 1400 °C

bead SiC whiskers were observed, and the granular materials (average particle size of 0.65  $\mu\text{m}$ ) on the whiskers were mainly composed of C, O, Si and Mg elements

(Fig. 2b).  $\text{Mg}_2\text{SiO}_4$  existed in a flaky morphology, and some  $\beta\text{-Si}_3\text{N}_4$  grains were embedded between flaky  $\text{Mg}_2\text{SiO}_4$  (Fig. 2c). For the sample SL containing micro- $\text{Al}_2\text{O}_3$

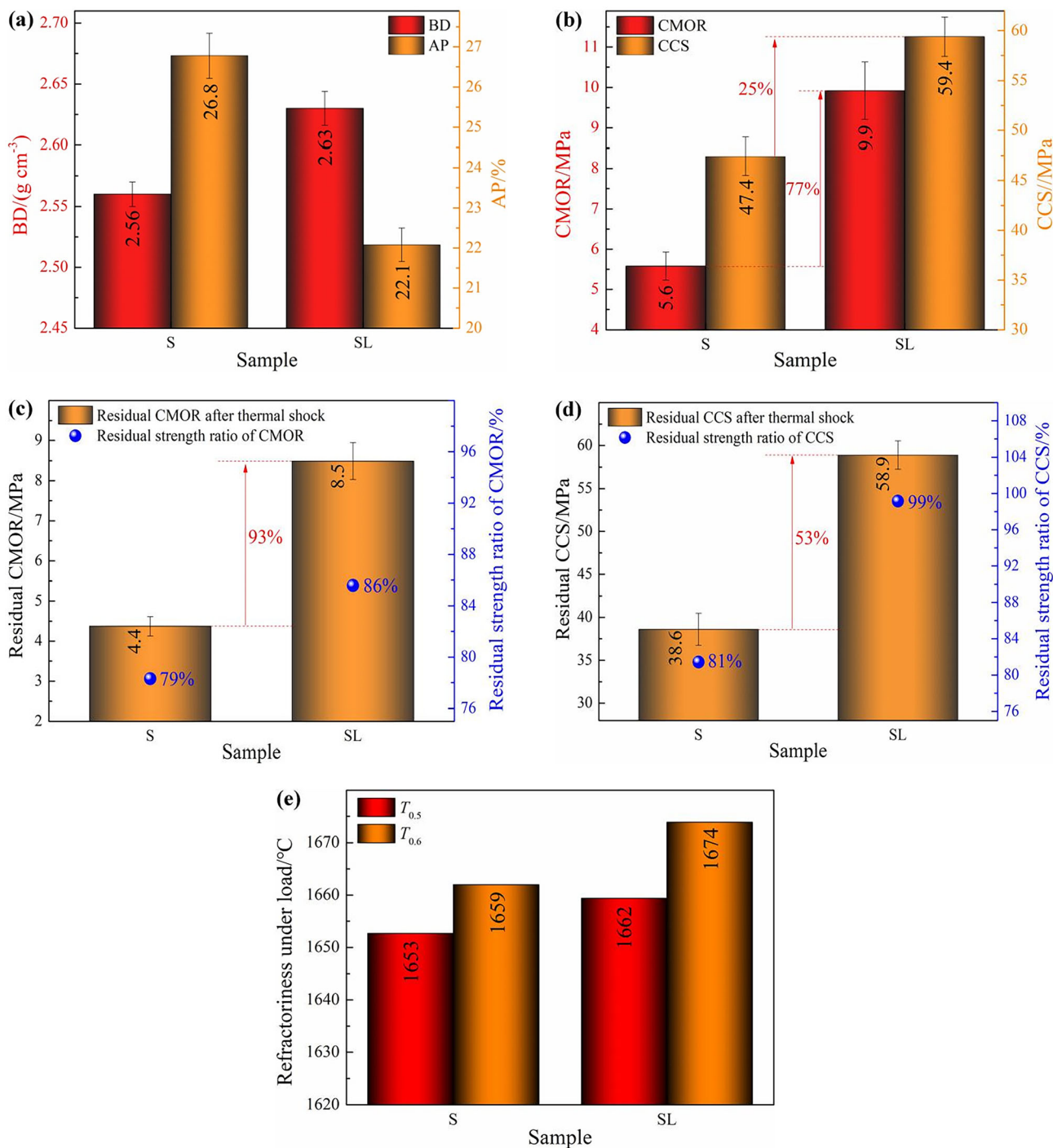


**Fig. 3** BD and AP (a), mechanical properties (b), residual CMOR and residual strength rate of CMOR (c), residual CCS and residual strength rate of CCS (d), and RUL (e) of samples S and SL nitrided at 1400  $^{\circ}\text{C}$

powders, the generated columnar  $\beta\text{-Si}_3\text{N}_4$  was distributed in a stepwise manner inside the sample (Fig. 2d, e). Specifically, large-sized  $\beta\text{-Si}_3\text{N}_4$  was distributed inside the hole, and small-grained  $\beta\text{-Si}_3\text{N}_4$  was distributed on the surface of the hole. Chain-bead SiC whiskers were observed (Fig. 2f), with increased size of the beads on the whiskers, and their average particle size was 0.71  $\mu\text{m}$ . The

size of flaky  $\text{Mg}_2\text{SiO}_4$  decreased, and its morphology was more regular. At the same time,  $\text{Mg}_2\text{SiO}_4$  also existed in a granular morphology, which was embedded between flaky  $\text{Mg}_2\text{SiO}_4$  to form an interlocked ceramic network structure (Fig. 2g–i). The knife-like  $\text{Si}_3\text{N}_4$  was also observed around the flaky  $\text{Mg}_2\text{SiO}_4$  (Fig. 2i), and some of its tips were fractured, which was due to the fact that the knife-like

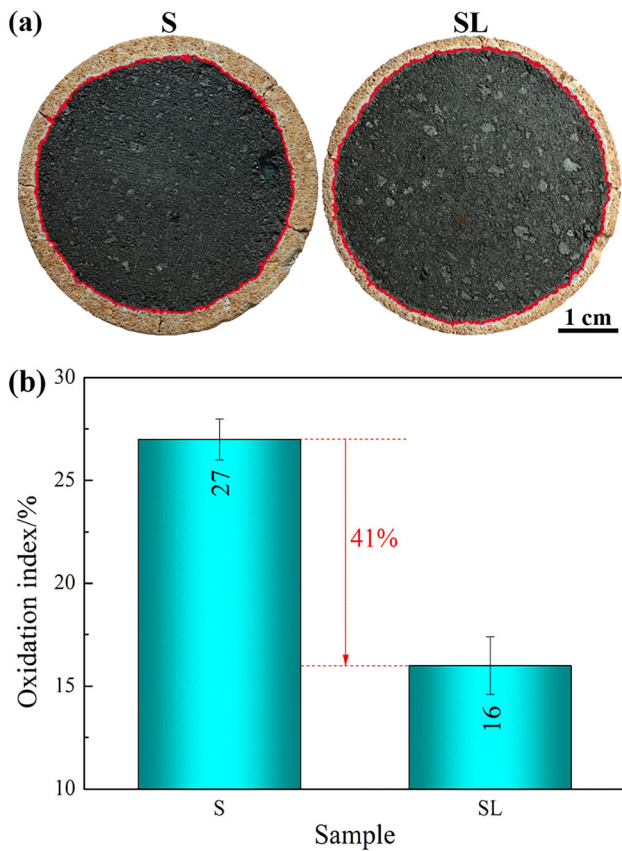
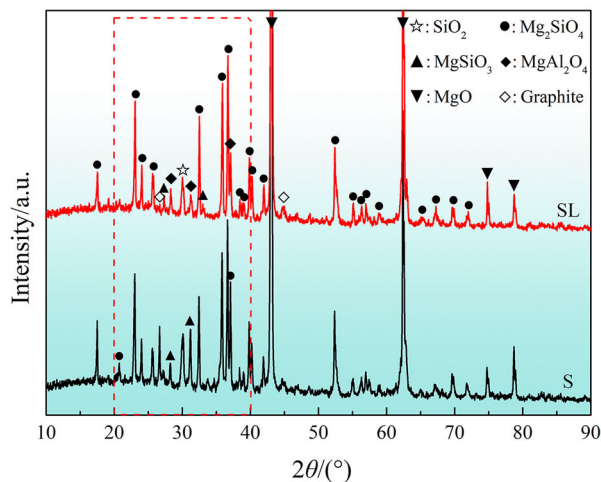


**Fig. 4** Cross-sections (a) and oxidation index (b) of nitrided samples S and SL after oxidation test at 1400 °C for 2 h in air

Si<sub>3</sub>N<sub>4</sub> was pulled out and broken under the action of external force. In addition, AlN existed in a coarse whisker-like morphology and was distributed in the pores (Fig. 2j), which could play a role in filling the pores.



### 3.2 Physical properties, thermal shock resistance, and refractoriness under load

Figure 3 shows the physical properties, thermal shock resistance, and refractoriness under load of nitrided samples S and SL. As shown in Fig. 3a, the addition of micro-Al<sub>2</sub>O<sub>3</sub> powders significantly increased the density of the sample, and the AP decreased from 26.8% to 22.1%. This is mainly because the small particle size of Al<sub>2</sub>O<sub>3</sub> powders could well fill the pores between particles. Moreover, the addition of micro-Al<sub>2</sub>O<sub>3</sub> powders promoted the formation of ceramic phases such as Mg<sub>2</sub>SiO<sub>4</sub> particles and small-sized Mg<sub>2</sub>SiO<sub>4</sub> flakes (Fig. 2), and the pores were filled [27]. Additionally, the inlaid structure formed between granular and flaky Mg<sub>2</sub>SiO<sub>4</sub>, columnar β-Si<sub>3</sub>N<sub>4</sub> with a stepped distribution, and Si<sub>3</sub>N<sub>4</sub> with a knife-like morphology optimized the internal structure of the material; thus, sample SL exhibited excellent mechanical strength and thermal shock resistance (Fig. 3b–d). The CMOR before and after thermal shock was 9.9 and 8.5 MPa, respectively, and their strengths were increased by 77% and 93% (strength change values: 4.3 and 4.1 MPa), respectively. The CCS before and after thermal shock was 59.4 and 58.9 MPa, respectively, and their strengths were increased by 25% and 53% (strength change values: 12.0 and 20.3 MPa), respectively. And the residual strength ratios of CMOR and CCS were up to 86% and 99%, respectively. As shown in Fig. 3e, sample SL exhibited a high RUL value, and its  $T_{0.6}$  was 1674 °C.

### 3.3 Oxidation behavior of MgO–C refractories

Figure 4 shows the cross-sections and oxidation indexes of nitrided samples S and SL after oxidation test at 1400 °C

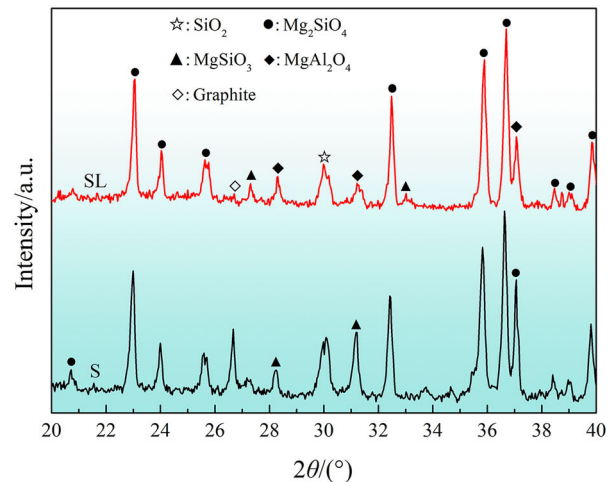


**Fig. 5** XRD patterns of oxidized decarburization area of nitrided samples S and SL after oxidation test at 1400 °C for 2 h in air

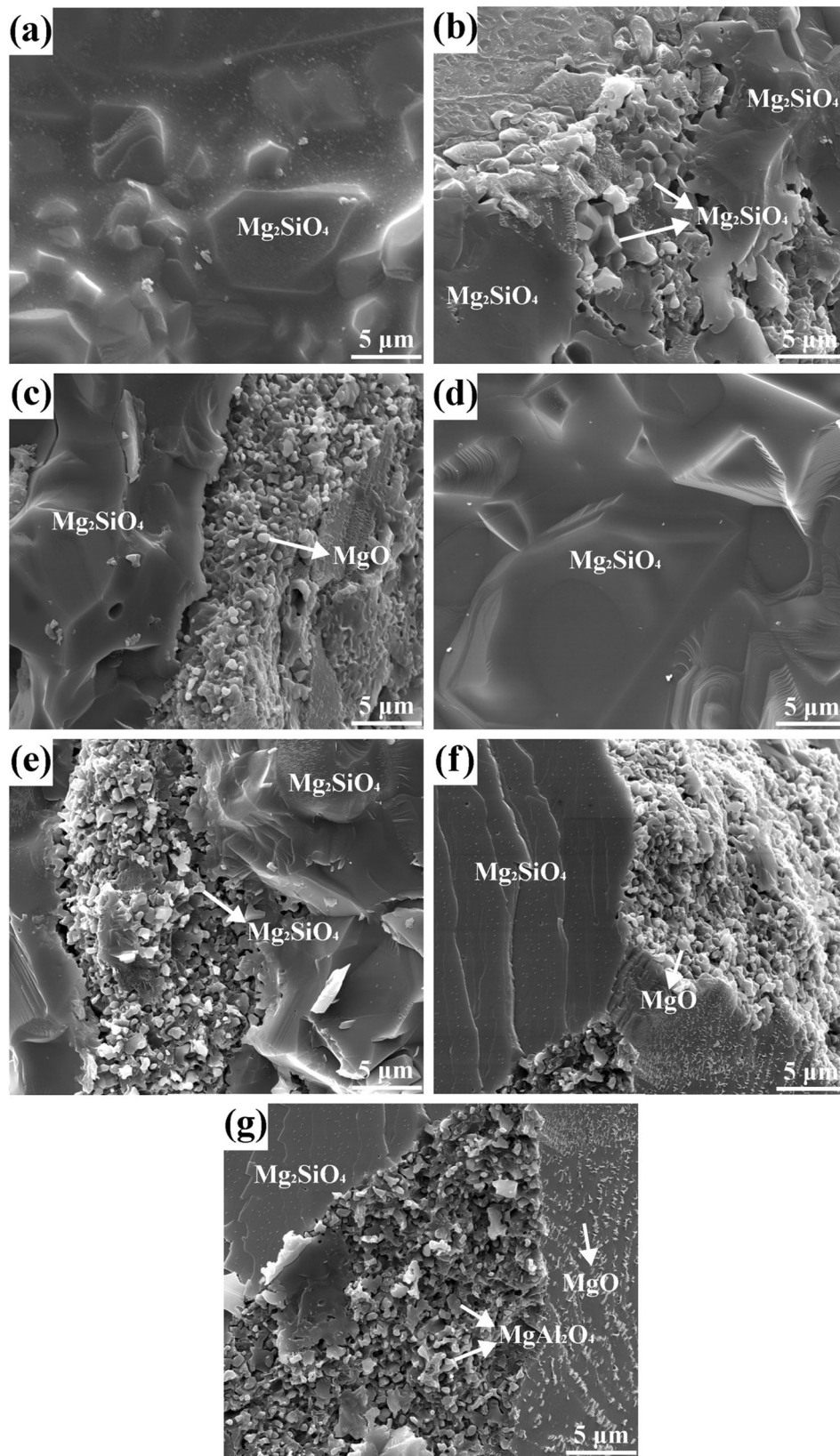


**Fig. 6** SEM images of oxidized decarburization area of nitrated samples S (a–c) and SL (d–g) after oxidation test at 1400 °C for 2 h in air

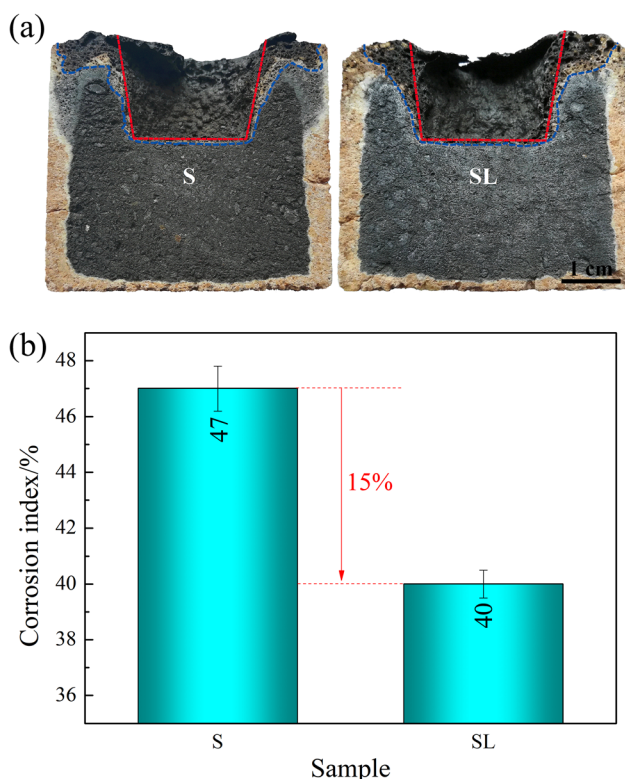
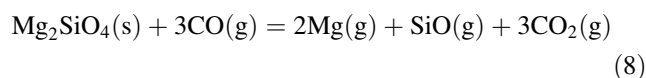
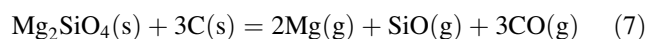
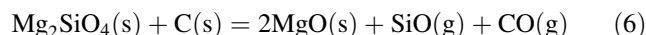
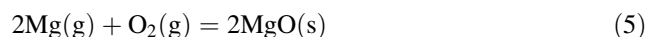
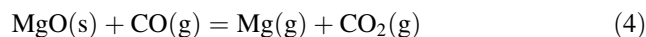
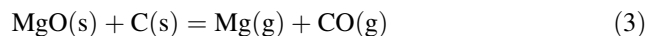


**Fig. 7** Cross-sections (a) and corrosion index (b) of nitrided samples S and SL after corrosion test at 1400 °C for 2 h in air

for 2 h. From Fig. 4a, it can be intuitively seen that sample SL containing micro-Al<sub>2</sub>O<sub>3</sub> powders had a thinner oxidation layer (yellow part), and there was a thicker oxidation transition layer (white part) between the oxidation layer and the original layer (black part). Compared with sample S without micro-Al<sub>2</sub>O<sub>3</sub> powders (oxidation index: 27%), the oxidation index of sample SL was only 16%, and the oxidation resistance was increased by 41% (Fig. 4b), showing excellent oxidation resistance.

The phase compositions of the oxidized decarburization layer area in Fig. 4a were detected, and the results are shown in Fig. 5. Compared with sample S, in addition to Mg<sub>2</sub>SiO<sub>4</sub>, MgSiO<sub>3</sub> and SiO<sub>2</sub> phases, a new phase of MgAl<sub>2</sub>O<sub>4</sub> was formed in the oxidized sample SL. SEM was used to further reveal the effect of micro-Al<sub>2</sub>O<sub>3</sub> addition on the oxidation resistance of samples, and the results are shown in Fig. 6. Figure 6a–c shows the SEM images of the oxidized decarburization area of nitrided sample S. It can be found that Mg<sub>2</sub>SiO<sub>4</sub> formed by oxidation existing in three morphologies: blocky Mg<sub>2</sub>SiO<sub>4</sub> wrapped by low melting point phases SiO<sub>2</sub> and MgSiO<sub>3</sub> (Fig. 6a), irregular large blocky Mg<sub>2</sub>SiO<sub>4</sub> covering on the surface of the matrix, and granular Mg<sub>2</sub>SiO<sub>4</sub> existing between the irregular large Mg<sub>2</sub>SiO<sub>4</sub> blocks (Fig. 6b, c). In addition, many MgO particles were also found (Fig. 6c), in which MgO

particles were mainly generated by the following ways: on the one hand, periclase was reduced to gaseous Mg by direct contact reaction with graphite or indirect reaction with CO gas generated by oxidation (reactions (3) and (4)). Subsequently, these Mg gas enriched around periclase reacted with external O<sub>2</sub> to form MgO (reaction (5)) [30]. On the other hand, the Mg<sub>2</sub>SiO<sub>4</sub> contained in the nitrided sample or the Mg<sub>2</sub>SiO<sub>4</sub> generated in the oxidation stage was reduced by graphite or CO gas to directly or indirectly generate MgO (reactions (5)–(8)) [31]. Compared with the microstructure of the oxidized sample S, the differences in the microstructure of the oxidized sample SL are as follows: the generated granular Mg<sub>2</sub>SiO<sub>4</sub> was smaller in size and more in amount (Fig. 6b, e); the blocky Mg<sub>2</sub>SiO<sub>4</sub> with a unique multi-step dense structure covered the surface of the matrix (Fig. 6f); in addition, many small particles of MgAl<sub>2</sub>O<sub>4</sub> were generated (Fig. 6g). Therefore, it is based on the fact that the fine particles (e.g., Mg<sub>2</sub>SiO<sub>4</sub>, MgAl<sub>2</sub>O<sub>4</sub> and MgO) were formed and effectively filled the pores, inhibiting the diffusion of O<sub>2</sub> into the interior of the sample. Moreover, the dense layer of Mg<sub>2</sub>SiO<sub>4</sub> with a multi-layered stepped structure formed by oxidation prevented further oxidation and improved the oxidation resistance of sample SL.



### 3.4 Corrosion behavior of MgO–C refractories

Figure 7 shows the cross-sections and corrosion indexes of nitrided samples S and SL after corrosion at 1400 °C for 2 h in air. As shown in Fig. 7a, both samples S and SL had a shallower slag corrosion depth after high-temperature corrosion, and a small amount of slag remained in the opening area of crucibles, but the corrosion area on both sides of the inner hole of sample S was larger. The corresponding corrosion index is shown in Fig. 7b. Compared with sample S (corrosion index: 47%), the addition of micro-Al<sub>2</sub>O<sub>3</sub> powders (sample SL) effectively improved the slag corrosion resistance, and its corrosion resistance was increased by 15%.

The backscattered electron (BSE) and energy dispersive spectroscopy (EDS) were used to further investigate the effect of micro-Al<sub>2</sub>O<sub>3</sub> addition on the corrosion resistance



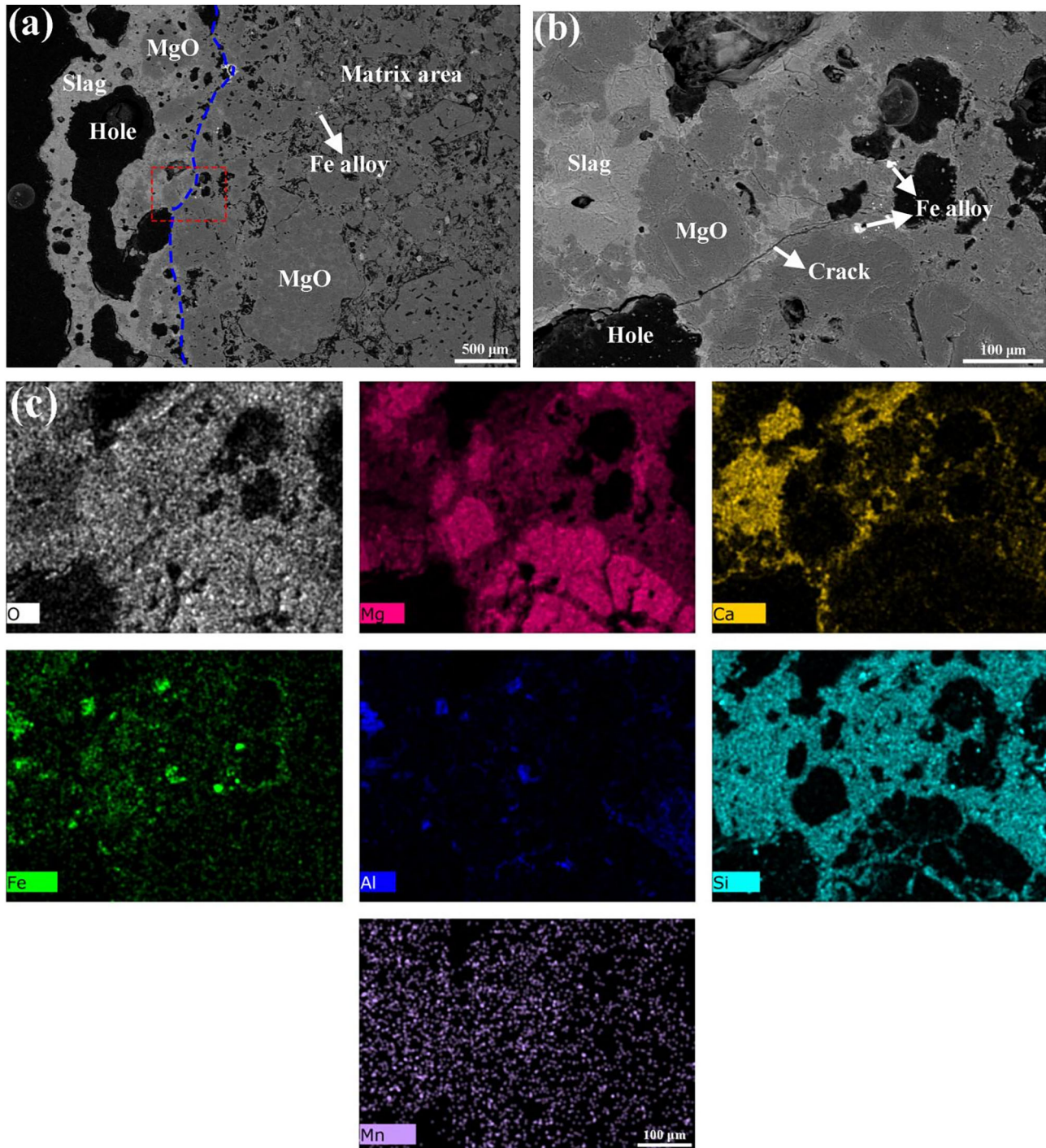


**Fig. 8** BSE images (a, b) of nitrided sample S after corrosion test and EDS mapping (c) of selected area

of the refractories (Figs. 8 and 9). As seen in Fig. 8a, under the corrosion of the slag, part of the MgO aggregates in sample S fell off and entered the slag. After corrosion, an erosion layer of about 1.45 mm was formed, and some Fe elements in the slag penetrated deeper into the refractory. The selected area (connection area between slag and refractory) in Fig. 8a was enlarged and observed. As can be

seen, MgO aggregates were seriously dissolved by the slag and lost their inherent contour (Fig. 8b). At the same time, due to the difference in the thermal expansion coefficient between the slag and MgO, microcracks were generated between the aggregates, and the slag was further penetrated into the refractory through microcracks [32]. The EDS mapping results in Fig. 8c showed that the Ca, Fe and Si

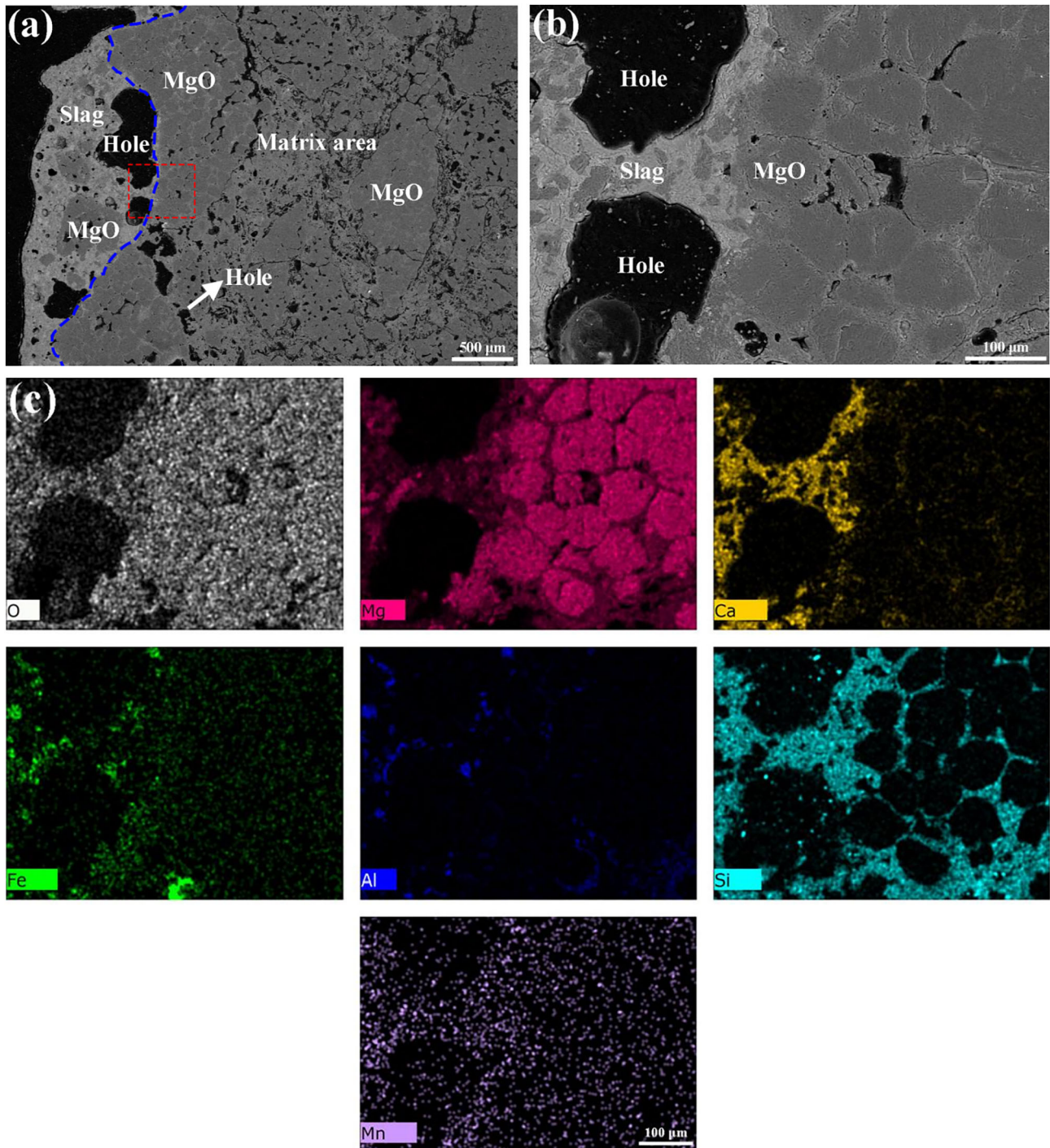


**Fig. 9** BSE images (a, b) of nitrided sample SL after corrosion test and EDS mapping (c) of selected area

elements in the slag were easy to diffuse and penetrate into the refractory and then reacted with MgO to form low melting point phases (e.g.,  $\text{CaMgSiO}_4$  and  $\text{Ca}_2\text{MgSi}_2\text{O}_7$ ) annular zone around the MgO aggregate, which aggravated the shedding of the aggregate.

Figure 9 shows the BSE images of corroded sample SL. As shown in Fig. 9a, erosion depth of the slag was 1.10 mm, and a small amount of MgO aggregate fell off into the slag. The connection area between slag and refractory was observed by magnification (Fig. 9b). It was

**Table 2** Comparison of properties of different low-carbon MgO–C refractories

Carbon source	Additive	Preparation condition	CMOR/MPa	CMOR <sub>res</sub> /MPa	CCS/MPa	CCS <sub>res</sub> /MPa	Oxidation index/%	Corrosion index/%	Source
2.5 wt.% graphite/carbon black	5 wt.% calcium magnesium aluminate and 5 wt.% SiC powder	1600 °C × 3 h, coking	7.7	–	–	–	73 (1600 °C × 3 h)	–	Ref. [36]
3 wt.% graphite	6 wt.% C/MgO nanocomposite powders	1400 °C × 3 h, coking	7.7	3.9 (1100 °C × 10 min, in air)	45.1	–	47 (1400 °C × 2 h)	18 (CaO/SiO <sub>2</sub> = 4.0, 1600 °C × 3 h)	Ref. [37]
2 wt.% graphite and 1 wt.% carbon black	0.5 wt.% ZrO <sub>2</sub> /Al <sub>2</sub> O <sub>3</sub> nanocomposite powders	1400 °C × 3 h, coking	~ 6.7	~ 6.0 (900 °C × 20 min, in oil)	–	–	32 (1400 °C × 3 h)	–	Ref. [38]
4 wt.% graphite	5 wt.% Al <sub>2</sub> O <sub>3</sub> /SiC composite powder	1400 °C × 3 h, coking	–	–	~ 58.0	~ 45.3 (1100 °C, in air)	~ 48 (1400 °C × 2 h)	–	Ref. [29]
4 wt.% graphite	1 wt.% SiC whiskers	1400 °C × 4 h, nitriding	8.9	7.2 (1100 °C × 30 min, in air)	67.8	57.3 (1100 °C × 30 min, in air)	–	50 (CaO/SiO <sub>2</sub> = 3.5, 1400 °C × 2 h)	Ref. [25]
5 wt.% graphite	1.5 wt.% Al <sub>2</sub> O <sub>3</sub> and 1.5 wt.% La <sub>2</sub> O <sub>3</sub>	1400 °C × 3 h, coking	–	–	70.5	66.5 (1100 °C × 20 min, in air)	51 (1400 °C × 1 h)	–	Ref. [22]
4 wt.% graphite	3 wt.% SiC whiskers and 2 wt.% Al <sub>2</sub> O <sub>3</sub> powder	1400 °C × 4 h, nitriding	9.9	8.5 (1100 °C × 30 min, in air)	59.4	58.9 (1100 °C × 30 min, in air)	16 (1400 °C × 2 h)	40 (CaO/SiO <sub>2</sub> = 3.5, 1400 °C × 2 h)	This work

Content in brackets indicates service condition of material; CMOR<sub>res</sub> is residual CMOR after thermal shock; CCS<sub>res</sub> is residual CCS after thermal shock; and CaO/SiO<sub>2</sub> is mass ratio of CaO/SiO<sub>2</sub> in slag

found that the MgO aggregates were closely connected at the connection area, and the aggregates were not seriously eroded and deformed. As seen in Fig. 9c, MgO aggregates were wrapped by Si, Al and O elements (Al element comes from slag and refractory), and a layer of isolation zone composed of forsterite and spinel was formed between MgO aggregates, which slowed down the penetration of slag. Combined with SEM and physical properties results (Figs. 2, 3a), the addition of micro-Al<sub>2</sub>O<sub>3</sub> powders optimized the internal structure of the material and significantly improved the density of the refractories, which reduced the passage of the slag into the refractories. In addition, since the refractory with micro-Al<sub>2</sub>O<sub>3</sub> powders itself contained Mg, Si and Al elements, forsterite and magnesia–aluminum spinel were formed in the refractory before the slag penetration (Fig. 5). These generated ceramic phases absorbed Mg, Al and Fe elements in the slag to form spinel and high-temperature solid solution [33–35], which increased the viscosity of the slag and inhibited the penetration of the slag. Therefore, it was observed that the easily erodent and penetrative Ca and Fe elements in the slag were effectively isolated by the tightly connected MgO aggregates. Compared with sample S, the sample SL showed excellent slag corrosion resistance. In a word, the addition of micro-Al<sub>2</sub>O<sub>3</sub> powders realized the synergistic improvement of mechanical strength, thermal shock, oxidation and corrosion resistances.

Additionally, we compared the properties of this work with other low-carbon MgO–C refractories [22, 25, 29, 36–38], and the results are shown in Table 2. The sample SL showed similar or good properties, especially the thermal shock and oxidation resistances were outstanding.

## 4 Conclusions

1. Compared with the refractories without micro-Al<sub>2</sub>O<sub>3</sub> powders, the addition of micro-Al<sub>2</sub>O<sub>3</sub> powders significantly improved the density of the refractories and optimized the formation and distribution of columnar β-Si<sub>3</sub>N<sub>4</sub> and granular and flaky Mg<sub>2</sub>SiO<sub>4</sub>. They synergistically improved the mechanical strength and thermal shock resistance of the refractories. The CMOR before and after thermal shock was increased by 77% and 93%, respectively, and the CCS before and after thermal shock was increased by 25% and 53%, respectively.
2. Under high-temperature service, the Mg<sub>2</sub>SiO<sub>4</sub>, MgAl<sub>2</sub>O<sub>4</sub> and MgO particles formed by oxidation in the refractories with micro-Al<sub>2</sub>O<sub>3</sub> powders effectively filled the pores, and the dense layer of Mg<sub>2</sub>SiO<sub>4</sub> with a stepped structure further hindered the entry of O<sub>2</sub>.

Moreover, the generated Mg<sub>2</sub>SiO<sub>4</sub> and MgAl<sub>2</sub>O<sub>4</sub> absorbed Mg, Al and Fe elements in the slag to form spinel and high-temperature solid solution. Consequently, the refractories with micro-Al<sub>2</sub>O<sub>3</sub> powders showed excellent oxidation and corrosion resistances, which were increased by 41% and 15%, respectively.

**Acknowledgements** The authors acknowledge financial support from the Scientific Research Fund of Hunan Provincial Education Department (22B0856), the Hengyang “Xiaohe” Science and Technology Talent Special Project ([2023]45), the Guidance Plan Project of Hengyang City ([2023]40), the National Natural Science Foundation of China (U20A20239), the College Students’ Innovation and Entrepreneurship Training Project (S202311528055), and the Characteristic Application Discipline of Material Science Engineering in Hunan Province ([2022]351). Moreover, the authors sincerely thank Prof. Zhi Wu at Hunan Institute of Technology for his guidance and help in the refractoriness under load test.

## Declarations

**Conflict of interest** The authors declare that they have no known competing financial interests or personal relationships that could have appeared to influence the work reported in this paper.

## References

- [1] Y.X. Luo, X. Wang, Z.L. Liu, C. Yu, C.J. Deng, J. Ding, J. Mater. Res. Technol. 27 (2023) 3632–3643.
- [2] M.Q. Liu, J.T. Huang, H.T. Meng, C. Liu, Z. Chen, H.Y. Yang, Z.J. Feng, X.B. Li, R.Y. Luo, Z.H. Huang, S.W. Zhang, J. Eur. Ceram. Soc. 43 (2023) 4198–4208.
- [3] X. Wang, C.J. Deng, J.H. Di, G.C. Xing, J. Ding, H.X. Zhu, C. Yu, J. Am. Ceram. Soc. 106 (2023) 3749–3764.
- [4] R.Q. Bai, S.Y. Liu, F.X. Mao, Y.Y. Zhang, X. Yang, Z.J. He, J. Iron Steel Res. Int. 29 (2022) 1073–1079.
- [5] Y.X. Wang, J. Liu, X.L. Tang, Y. Wang, H.W. An, H.H. Yi, Resour. Conserv. Recycl. 194 (2023) 106994.
- [6] X. Yu, C. Tan, Global Environ. Change 76 (2022) 102574.
- [7] Z.X. Ji, W.J. Liu, N. Liao, Y.W. Li, T.B. Zhu, J. Iron Steel Res. Int. 29 (2022) 1129–1137.
- [8] X.M. Ren, B.Y. Ma, S.M. Li, H.X. Li, G.Q. Liu, W.G. Yang, F. Qian, S.X. Zhao, J.K. Yu, J. Iron Steel Res. Int. 28 (2021) 38–45.
- [9] S.E. Gass, P.G. Galliano, A.G.T. Martinez, J. Eur. Ceram. Soc. 41 (2021) 3769–3781.
- [10] J.Y. Luo, X.M. Ren, X.C. Chong, D.H. Ding, B.Y. Ma, G.Q. Xiao, J.K. Yu, J. Iron Steel Res. Int. 29 (2022) 1041–1051.
- [11] Y. Chen, J. Ding, C.J. Deng, C. Yu, Ceram. Int. 49 (2023) 26871–26878.
- [12] Q. Gu, T. Ma, F. Zhao, Q.L. Jia, X.H. Liu, G.Q. Liu, H.X. Li, J. Alloy. Compd. 847 (2020) 156339.
- [13] C. Yu, B. Dong, Y.F. Chen, B.Y. Ma, J. Ding, C.J. Deng, H.X. Zhu, J.H. Di, J. Iron Steel Res. Int. 29 (2022) 1052–1062.
- [14] Y. Chen, C.J. Deng, X. Wang, C. Yu, J. Ding, H.X. Zhu, J. Eur. Ceram. Soc. 41 (2021) 963–977.
- [15] Y.X. Luo, X. Wang, Z.L. Liu, C. Yu, C.J. Deng, J. Ding, J. Alloy. Compd. 975 (2024) 172937.
- [16] X.C. Chong, G.Q. Xiao, D.H. Ding, J.Y. Luo, P.Y. Yan, C. Zou, X. Hou, Ceram. Int. 49 (2023) 31752–31762.

- [17] Z.L. Liu, C.J. Deng, C. Yu, J. Ding, H.X. Zhu, *Ceram. Int.* 49 (2023) 29104–29113.
- [18] Y.J. Zhao, G.Q. Li, Y. Wu, C. Yuan, Z. Meng, X.X. Deng, Y. Liu, *J. Iron Steel Res. Int.* (2023) <https://doi.org/10.1007/s42243-023-01056-7>.
- [19] C. Yu, J. Ding, C.J. Deng, H.X. Zhu, N. Peng, *Ceram. Int.* 44 (2018) 1104–1109.
- [20] Y. Chen, C.J. Deng, X. Wang, J. Ding, C. Yu, H.X. Zhu, *Constr. Build. Mater.* 240 (2020) 117964.
- [21] Q. Gu, Y.X. Zhang, W.K. Ma, G.Q. Liu, X.H. Liu, H.X. Li, *Ceram. Int.* 47 (2021) 2705–2714.
- [22] X.M. Ren, B.Y. Ma, H. Liu, Z.F. Wang, C.J. Deng, G.Q. Liu, J.K. Yu, *J. Eur. Ceram. Soc.* 42 (2022) 3986–3995.
- [23] Y. Chen, X. Wang, C.J. Deng, C. Yu, J. Ding, H.X. Zhu, *Constr. Build. Mater.* 289 (2021) 123032.
- [24] X. Wang, Y. Chen, J. Ding, C. Yu, C.J. Deng, H.X. Zhu, *Ceram. Int.* 47 (2021) 10603–10610.
- [25] Y. Chen, J. Ding, C. Yu, X.M. Lou, Z. Wu, C.J. Deng, *J. Phys. Chem. Solids* 177 (2023) 111304.
- [26] S. Ghasemi-Kahrizsangi, H. Gheisari Dehsheikh, M. Boroujerdnia, *Mater. Chem. Phys.* 189 (2017) 230–236.
- [27] K. Su, Q. Zhang, X.K. Tian, D.Z. Ouyang, X.H. Liu, J.Y. Cui, *Ceram. Int.* 49 (2023) 23696–23703.
- [28] D.H. Ding, X.C. Chong, G.Q. Xiao, L.H. Lv, C.K. Lei, J.Y. Luo, Y.F. Zang, *Ceram. Int.* 45 (2019) 16433–16441.
- [29] B.Y. Ma, X.M. Ren, Z. Gao, F. Qian, Z.Y. Liu, G.Q. Liu, J.K. Yu, G.F. Fu, *J. Iron Steel Res. Int.* 29 (2022) 1080–1088.
- [30] Z.Y. Liu, J.K. Yu, S.J. Yue, D.B. Jia, E.D. Jin, B.Y. Ma, L. Yuan, *Ceram. Int.* 46 (2020) 3091–3098.
- [31] H.J. Duan, H.X. Zhu, C.J. Deng, W.J. Yuan, J. Li, *Int. J. Mater. Res.* 104 (2013) 586–589.
- [32] X. Qi, L. Zhang, X.D. Luo, S.Y. Wang, J.G. You, G.Q. Ding, Y. Zheng, J.L. Zhao, Y.P. Zhou, Z.Z. Pan, *Ceram. Int.* 49 (2023) 15122–15132.
- [33] T. Preisker, P. Gehre, G. Schmidt, C.G. Aneziris, C. Wöhrmeyer, C. Parr, *Ceram. Int.* 46 (2020) 452–459.
- [34] H.T. Zhong, B.Q. Han, J.W. Wei, Y.W. Wei, W. Yan, N. Li, Z. Miao, K.G. Zhang, *Ceram. Int.* 49 (2023) 2026–2033.
- [35] M.Y. Yang, G.Q. Xiao, D.H. Ding, J.Z. Zhao, W. Zhao, D.A. Yang, L. Liu, L. Ren, X.T. Zhao, L. Gong, *Ceram. Int.* 48 (2022) 24411–24420.
- [36] W.J. Guo, T.B. Zhu, X. Zhao, Y.W. Li, Q.L. Chen, X.F. Xu, Y.B. Xu, Y.J. Dai, W. Yan, *J. Eur. Ceram. Soc.* 44 (2024) 496–509.
- [37] X.C. Chong, K.D. Li, G.Q. Xiao, D.H. Ding, X. Hou, *Ceram. Int.* 49 (2023) 34316–34326.
- [38] Q.L. Chen, T.B. Zhu, Y.W. Li, Y. Cheng, N. Liao, L.P. Pan, X. Liang, Q.H. Wang, S.B. Sang, *Ceram. Int.* 47 (2021) 20178–20186.

Springer Nature or its licensor (e.g. a society or other partner) holds exclusive rights to this article under a publishing agreement with the author(s) or other rightsholder(s); author self-archiving of the accepted manuscript version of this article is solely governed by the terms of such publishing agreement and applicable law.